INORGANIC CHEMISTRY FRONTIERS

RESEARCH ARTICLE

View Article Online
View Journal

Cite this: DOI: 10.1039/d6qi00728g

Deciphering the excited-state landscape of Cr(III) tris(diimines) using $[Cr(phen)_3]^{3+}$

Alexandra T. Barth, †[a] Dilara Farkhutdinova, †[b,c] Adrienne P. Faulkner, [a] Irene Y. Dzaye, [a] Jonathan P. Wheeler, [a] Leticia González *[b] and Felix N. Castellano *[a]

Received 8th April 2026,
Accepted 12th April 2026

DOI: 10.1039/d6qi00728g

rsc.li/frontiers-inorganic

Earth-abundant Cr(III) polypyridines chromophores feature long-lived doublet ligand-field excited states. The thermally equilibrated $^2T_1/^2E$ ligand-field excited state manifold produces broad, structured UV-Vis-NIR absorption bands. Although ubiquitous across pseudo-octahedral Cr(III) diimine complexes, the dynamics and individual electronic transitions underlying these spectra have remained elusive. Here, we combine time-resolved spectroscopy and multiconfigurational calculations to assign ground- and excited-state absorption spectra of Cr(III) tris(1,10-phenanthroline), $[Cr(phen)_3]^{3+}$, as a prototypical example for this class of complexes. Excited-state kinetics reveal a rapid biexponential decay of the initially prepared intraligand/ligand-to-metal charge transfer [$^4(^1IL)/^4LMCT$] excited state into the lowest $^2T_1/^2E$ state within 10 picoseconds, assigned to intersystem crossing and vibrational relaxation. Calculations identify broad excited-state absorption features associated with metal-centered ligand-field states (^2MC) mixed with intraligand (^2IL) transitions within the doublet manifold. These results provide detailed spectral assignments and highlight the need to include multiconfigurational ligand-based orbitals when modeling the spectral properties of Cr(III) coordination complexes.

1. Introduction

Photocatalysis has pioneered novel strategies in modern organic synthesis, enabling the generation of valuable small molecules and targeted late-stage functionalization.[1–9] The photosensitizers typically used for these applications are long-lived triplet metal-to-ligand charge transfer (^3MLCT) excited states, which leverage the potent excited-state redox potentials of Ru(II) and Ir(III) complexes to drive these transformations.[1,10,11] Because these metals are rare, expensive, and environmentally scarce, it is valuable to identify earth-abundant alternatives that feature similar excited-state reactivity without sacrificing catalytic performance.[12–18] Both homo- and heteroleptic Cr(III) pseudo-octahedral complexes have become popular candidates in this regard,[19–35] given their long-lived intraconfigurational spin-flip excited states, which are prompted by initial light activation into persistent metal-centered (MC) doublet excited states.[36–66] However, the relaxation processes emanating from the initially prepared charge-transfer excited states remain elusive, and the relaxed doublet excited states possess rather large extinction coefficients that are inconsistent with being solely derived from LF transitions.[67–70] Prior efforts have modeled the excited-state landscapes of related Cr(III) chromophores with notable success, primarily focusing on metal-centered intermediates.[38,52,53] Despite these advancements, the origin of the broad, excited-state absorption profile generated within the Cr(III) doublet manifold remains unclear.[51]

Herein, we report a synergistic experimental and computational investigation into the prototypical Cr(III) tris(diimine) complex $[Cr(phen)_3]^{3+}$ (**1**), where phen = 1,10-phenanthroline (Scheme 1). By combining ultrafast time-resolved spectroscopy with state-of-the-art multiconfigurational calculations, we assign the ground- and excited-state spectra of the benchmark complex and elucidate the nature of the underlying electronic transitions. This effort represents an advancement over prior efforts by enabling the resolution of complex multiconfigurational excited states. Through the lens of this prototypical complex, we aim to provide a unified and comprehensive understanding of excited-state electronic transitions in Cr(III) diimine chromophores, establishing a general framework for interpreting their excited-state absorption features and, consequently, their overall photophysics.

[a]Department of Chemistry, North Carolina State University, Raleigh, North Carolina, 27695-8204, USA. E-mail: fncastel@ncsu.edu
[b]Institute of Theoretical Chemistry, Faculty of Chemistry, University of Vienna, Währinger Straße 17, 1090 Vienna, Austria. E-mail: leticia.gonzalez@univie.ac.at
[c]Doctoral School in Chemistry (DosChem), University of Vienna, Währinger Straße 38, 1090 Vienna, Austria
† Equal authorship contribution.

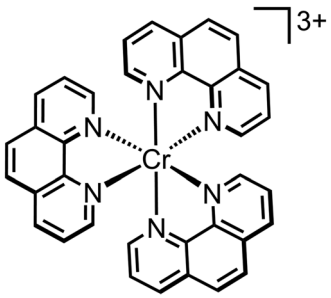

1

Scheme 1 Molecular structure of $[Cr(phen)_3]^{3+}$ (**1**).

2. Results and discussion

The static UV-visible absorption profile of **1** serves as a foundational probe into the complex electronic landscape of the quartet manifold, where distinct energetic regions reflect the interplay between ligand-based charge transfer and metal-centered transitions. The electronic absorption spectrum of the six-coordinate pseudo-octahedral $[Cr(phen)_3](BF_4)_3$ (**1**) dissolved in acetonitrile (295 K) is presented in Fig. 1A. The spectrum matches prior measurements in acidified aqueous solutions.[47,59] This spectrum exhibits three regions with distinct spectral intensities: a high-intensity band at 267 nm assigned as an intraligand $^1(\pi\text{–}\pi)^*$ transition, denoted $^4(^1IL)$ to illustrate quartet spin multiplicity on the metal and singlet on the phen ligand; a broad region spanning from 282 to 355 nm with moderate intensity, attributed to spin-allowed ligand-to-metal charge transfer (^4LMCT) transitions mixed with $^4(^1IL)$ and $^4T_1$ ligand-field states; and weak transitions arising from spin-allowed ligand-field transitions into the $^4T_2$ state, which extend into the visible region (Fig. 1A inset). The observed electronic transitions and their characterization are summarized in Table 1.

The assignment is based on vertical excitations computed with the multiconfigurational restricted active space self-consistent field (RASSCF) method and an active space of (13,3,3;5,5,7), comprising 13 electrons distributed over 17 orbitals (see Computational details). Multiconfigurational methods are mandatory for treating the complex manifolds of open-shell transition-metal complexes and circumventing the significant spin-contamination issues encountered with single-reference density functional theory. The active space was carefully determined through convergence of the relevant excited states and by benchmarking against the experimental spectrum. It includes 3 π and 2 σ orbitals in the RAS1 subspace, the full set of 3d metal orbitals in the RAS2 subspace, and 3 π* and 1 σ* orbitals, as well as three 4d orbitals in the RAS3 subspace (Fig. 2). Related active spaces have been widely applied to transition-metal complexes and are known to provide a reliable treatment of non-dynamic electron correlation.[53,71,72] On the basis of these RASSCF calculations, we determined that the fine structure superimposed on the LMCT and IL bands originates from contributions from ^4MC states, as listed in Table 1 and Table S2.

Upon UV- or visible blue light excitation of **1**, excited quartet states are initially populated, undergo rapid intersystem crossing, and then are well-established to populate an emissive doublet manifold composed of two thermally equilibrated states, $^2T_1/^2E$ (Φ_{PL} = 0.66% in anaerobic CH_3CN at 295 K).[54–58] Photoluminescence (PL) emission from $^2T_1/^2E$ in **1** was measured in acetonitrile at 295 K and in *n*-butyronitrile at 77 K as presented in Fig. 1B and C, respectively. The PL emission maxima remain unperturbed at low temperatures, indicating that the electronic and geometric structures are similar

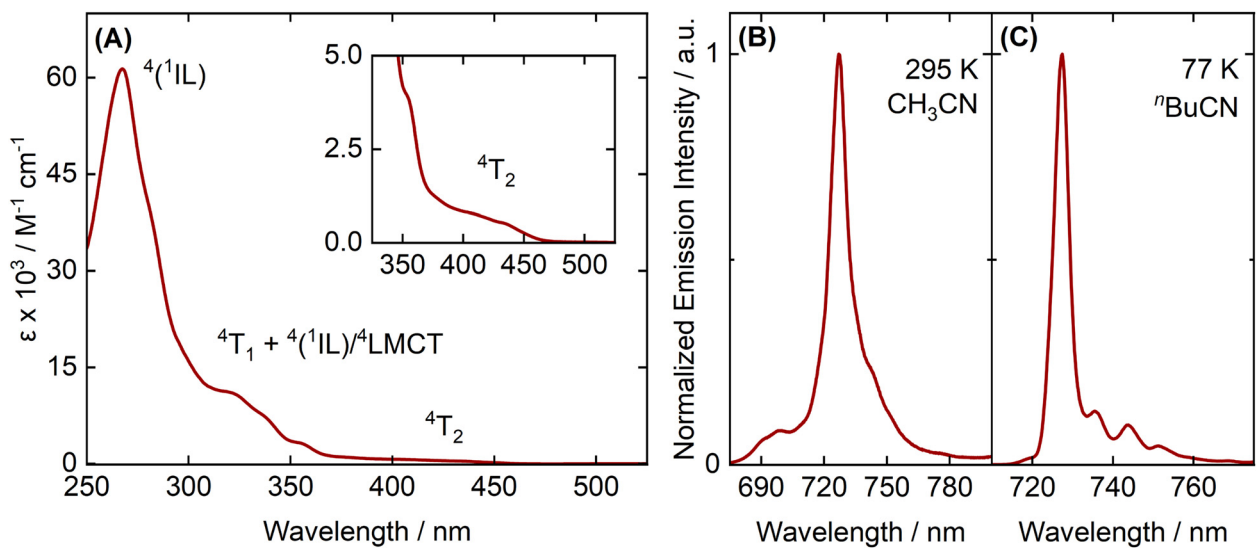

Fig. 1 Absorption and PL emission (λ_{ex} = 355 nm) properties of **1**. The absorption (A) and PL emission (B) profiles were recorded at 295 K in CH_3CN. The PL emission (C) profile at 77 K was recorded in *n*-butyronitrile.

Table 1 Experimental and RASSCF(13,3,3;5,5,7) absorption and PL emission parameters of **1**

λ_{abs} [a,b] {ε}[c]	Calc. λ_{abs} [d] {f_{osc}}[e]	Assignment	λ_{em} [a,b]	λ_{em} [b,f]	Calc. λ_{em} [d]	Assignment
—	261{3.2×10^{-2}}	$^4(^1IL) + {}^4LMCT$				
267 {61 300}	262{1.7×10^{-2}}	$^4(^1IL)$				
—	276 {1.0×10^{-3}}	^4LMCT				
282 {37 700}, sh	284 {6.2×10^{-4}}	$^4T_1$				
—	309 {1.1×10^{-4}}	$^4T_1$				
—	313 {2.5×10^{-5}}	$^4T_1$	699			$^2T_1$
323 {12 000}, sh	319 {6.2×10^{-4}}	$^4T_1$	727	727	630	^2E
338 {8120}, sh	333 {1.1×10^{-2}}	$^4(^1IL) + {}^4LMCT$				
355 {3890}, sh	—	$^4(^1IL) + {}^4LMCT$				
404 {809}, sh	420 {2.1×10^{-5}}	$^4T_2$				
435 {513}, sh	437 {7.2×10^{-5}}	$^4T_2$				
454 {219}, sh	443 {7.5×10^{-5}}	$^4T_2$				

[a] Recorded at 295 K in MeCN. [b] Wavelength in nm. [c] Extinction coefficient in M^{-1} cm^{-1}. [d] Calculated RASSCF(13,3,3;5,5,7) vertical excitation energies in nm. [e] Transition oscillator strength. [f] Recorded at 77 K in ^{n}BuCN.

and essentially temperature-independent. Computational modeling reproduces the PL experimental data of this chromophore with high accuracy, see Table 1 and Table S4. Accordingly, we attribute the lowest ^2E state as the dominant contributor to the PL at 727 nm and RT with a shoulder originating from thermally activated $^2T_1$ emission centered at 699 nm. The PL excitation scan at RT centered on the doublet emission features reproduces the absorption spectrum of **1** (Fig. S1).

To precisely quantify the structural reorganization accompanying the quartet-to-doublet spin conversion, we interrogated the photoluminescence (PL) properties at cryogenic temperatures, where suppression of thermal fluctuations reveals the underlying vibronic landscape. In *n*-butyronitrile glass at 77 K, thermal activation of the $^2T_1$ state is completely suppressed, evidenced by the disappearance of the high-energy shoulder PL in Fig. 1B and isolation of the radiative ^2E PL at lower energy (Fig. 1C). The minimal thermal broadening at 77 K yields a vibronic progression that originates from changes experienced in the excited-state geometry. The total displacement and individual bond distortions in the excited state can be determined from the vibrational fine structure in the 77 K emission spectrum. These features illustrate the interaction between the displaced excited-state potential energy surface and the ground-state vibrational modes along the normal mode coordinate. The average low-frequency peak-to-peak separation of 148 cm^{-1} observed in **1** is well-represented by the A_1 symmetric stretching mode at 145 cm^{-1}, as predicted by DFT calculations (Table S1). This suggests that the primary distortion occurring in the excited state is along the A_1 normal mode coordinate. The magnitude of electron-phonon coupling can be determined from the intensity of these features, as represented by the Huang–Rhys parameter (S_{HR}). With an S_{HR} value of 0.131, a total normal mode displacement (ΔQ) of 0.0222 Å, and Cr–N bond displacements (Δr) of 0.009 Å, geometric distortion and spin conversion appear to be weakly coupled in **1**.

The excited-state dynamics of **1** in CH_3CN were monitored using ultrafast transient absorption spectroscopy and time-resolved PL emission intensity decay measurements (Table 2). Upon 355 nm pulsed laser excitation, there was a prompt generation of two distinct excited state absorption (ESA) spectral features in the visible region of the difference spectrum (Fig. 3A), along with another broad ESA feature spanning across the near-infrared range extending to the limit of our detection range (1600 nm, shown in Fig. 3B). This excited state difference profile is dissimilar from the profile of the one-electron reduced ligand accessed from spectroelectrochemistry measurements (Fig. S2 and S3) and does not map onto the visible or near-IR absorption difference spectra of the ^{3}MLCT state in the related $[Ru(phen)_3]^{2+}$ species (Fig. S4 and S5), which suggests that this is not an MLCT excited state. The broadness and intensity of these excited-state absorption features ($\varepsilon^*_{max} = 3000\,M^{-1}\,cm^{-1}$, Fig. S6) suggest a spin-allowed charge-transfer transition into a mixed $[^4(^1IL)/^4CT]$ state.[49,73]

The early-time kinetic evolution provides a window into the rapid non-radiative pathways that bypass the initial charge-transfer states in favor of metal-centered configurations.[73] In the visible region, the initially broad ESA feature at 460 nm decays rapidly within the first picosecond, accompanied by the narrowing of a band around 530 nm. A similar kinetic evolution is observed in the near-infrared region, where a broad ESA feature centered at 1030 nm diminishes rapidly over a comparable sub-picosecond timescale. This decay is more pronounced at lower-energy probe wavelengths across the NIR region, which matches the rapid 50 fs decay observed by McCusker and coworkers in $Cr(acac)_3$ at red probe wavelengths (650 nm).[49] These dynamics are consistent with an intersystem crossing from the initially populated quartet state into the lower-energy metal-centered doublet manifold.[74] The prompt nature of this relaxation, coupled with minimal spectral reshaping, suggests modest structural reorganization and efficient coupling between the initial charge-transfer state and the final metal-localized $^2E/^2T_1$ states.

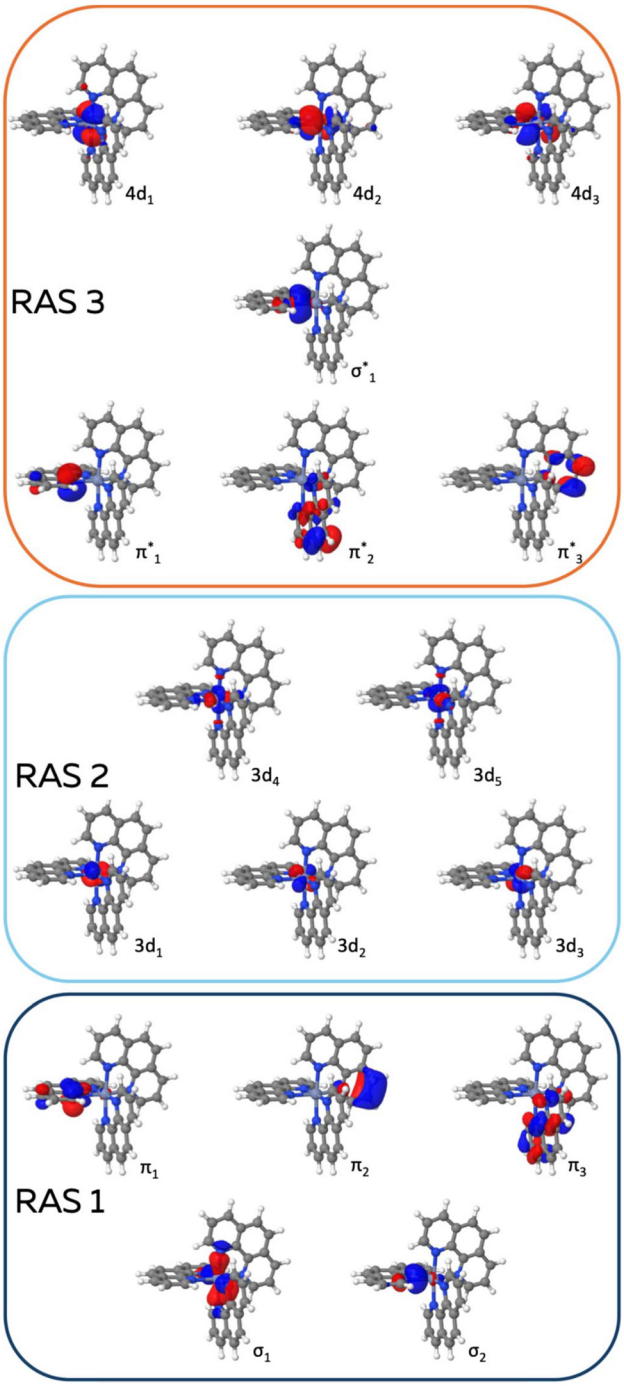

Fig. 2 RASSCF (13,3,3;5,5,7) active space natural orbitals for compound **1**. The protocol includes three π and two σ orbitals in the RAS1 subspace, the full set of 3d metal orbitals in the RAS2 subspace, three π* and one σ* orbitals, and three 4d orbitals in the RAS3 subspace. The colored contouring illustrates the subdivision into different active spaces, while black labels indicate the orbital types.

Following this rapid intersystem crossing, the system enters a secondary relaxation phase characterized by vibrational cooling and structural equilibration. This slower process unfolds over the 1–8 ps window. During this time period, the ESA in both the visible and NIR regions continues to decrease in intensity and evolves into a spectrum with sharp, well-defined features. In the visible range, the transitions at 375 nm and 515 nm become more prominent, while the NIR spectrum resolves into a broad feature centered at 1200 nm. This sharpening and modest blue shift in spectral features are consistent with vibrational relaxation within the metal-centered manifold.[75] The spectral data from this analysis support a sequential decay model, in which a fast event is followed by a slower vibrational relaxation.

The completion of these ultrafast processes yields a remarkably persistent, thermally equilibrated excited state that defines the photophysics of **1** and persists for hundreds of microseconds. Beyond 30 ps, the difference spectrum remains unchanged, indicating that the excited-state evolution of **1** has completed, terminating on the $^2T_1/^2E$ surfaces as a long-lived excited state. This relaxed excited state is populated irrespective of the excitation wavelength (Fig. S7–S11); however, excitation at higher pump energies (320–360 nm) leads to faster relaxation dynamics relative to lower pump energies (400 and 435 nm) (Fig. S12). This excitation wavelength dependence suggests that higher-energy excitation accesses states farther removed from the $^4T_2$ potential energy surface, thereby accelerating internal conversion and subsequent relaxation processes.[67]

The persistent $^2T_1/^2E$ state is thermally equilibrated, and its excited-state lifetime was determined from time-resolved photoluminescence experiments. As presented in Fig. 3C, the depopulation of the lowest doublet excited states occurs uniformly. In deaerated CH_3CN at 295 K, **1** exhibits an excited state lifetime of 199 ± 3 μs, which is slightly shorter but consistent with the reported value of 270 μs originally measured in aqueous HCl.[50] Despite the lifetime difference, the excited state remains sufficiently long-lived to mediate energy and electron transfer processes.

To definitively assign the electronic origins of this long-lived state, we benchmarked the experimental ESA features against our RASSCF calculations, using the computational scheme described above.

The electronic transitions originating from this excited state across the UV-Vis-NIR range, shown in Fig. 3A and B, are assigned based on RASSCF(13,3,3;5,5,7) calculations, which model the absorption profile from the doublet minima into the doublet excited states manifold. The experimental and calculated excited state absorption spectra are shown in Fig. 4.

The electronic absorption spectrum is characterized by two primary features. The first feature, a broad band centered at approximately 511 nm, corresponds to an electronic transition into a state with predominantly MC character. This is followed by a second, significantly more intense feature at approximately 370 nm, assigned to a doublet state with mixed MC and IL character.

Analysis of configuration interaction coefficients (Table S3) reveals that the primary electronic redistribution involves the promotion of an electron from the RAS1 π_2 orbital into the

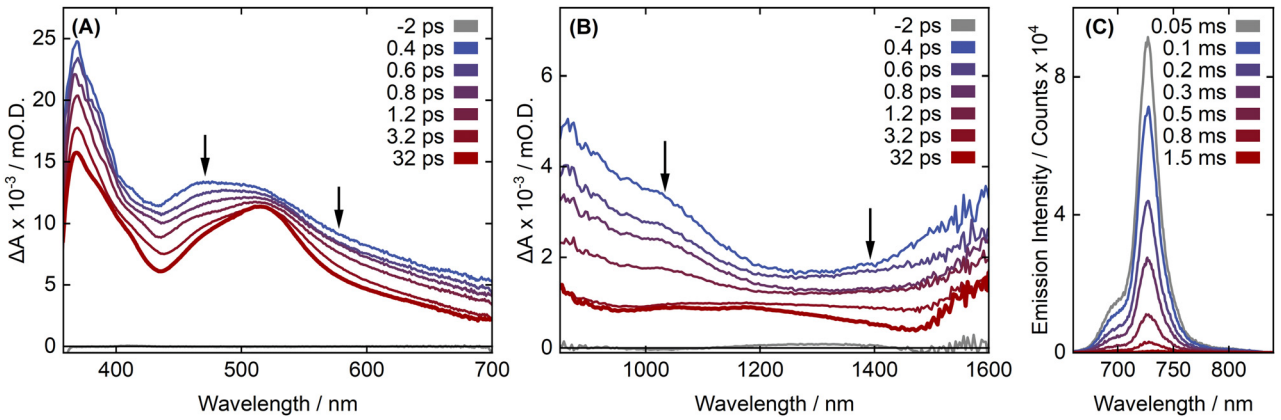

Fig. 3 Ultrafast transient absorption spectra in the UV-visible (A) and near-infrared (B) regions illustrate the sequential nonradiative relaxation within the excited-state manifold, which leads to population of the long-lived $^2T_1/^2E$ excited state (λ_{ex} = 355 nm; P = 0.5 μJ per pulse; 100 fs fwhm). Time-resolved photoluminescence data (C) show the radiative decay of this state under nanosecond-pulsed laser excitation (λ_{ex} = 355 nm; 8.2 mJ per pulse; 7 ns fwhm). All measurements were recorded in CH_3CN at 295 K.

Table 2 Time-resolved absorption and photoluminescence data for **1** measured at 295 K in acetonitrile

	Visible (400–700 nm)		Near-IR (850–1600 nm)		Photoluminescence
Species	τ_1 (ps)	τ_2 (ps)	τ_1 (ps)	τ_2 (ps)	τ_{PL} (μs)
1	0.23 ± 0.02	1.6 ± 0.4	0.38 ± 0.16	1.5 ± 0.6	199 ± 3

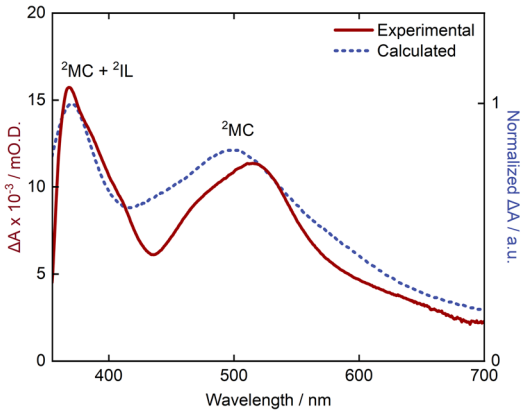

Fig. 4 Experimental (solid red line) and calculated (dashed blue line) excited-state absorption (ESA) spectra for **1**. The theoretical spectrum was obtained *via* RASSCF vertical excitations from the lowest-lying doublet state, applying a Gaussian broadening with a FWHM of 0.5 eV. The broad features are assigned to a complex mixing of MC and IL transitions. The experimental spectrum is measured from a delay time of 32 ps (λ_{ex} = 355 nm; P = 0.5 μJ per pulse; 100 fs fwhm).

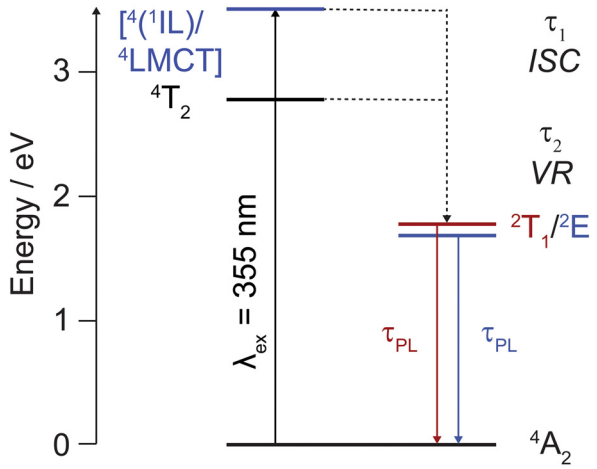

Fig. 5 Proposed excited state cascade for **1** in CH_3CN, including key electronic transitions and metal-centered phosphorescence (τ_{PL}) in the near-IR.

RAS3 π_3^* orbital, along with transitions within the d-orbital manifold (see Fig. 2). The simultaneous participation of both the d-manifold and the ligand π-system in these orbitals highlights the strong electronic communication between the metal center and the ligand framework. The transition energies show excellent agreement with experimental maxima. Calculated vertical excitation energies for the doublet manifold are presented in Table S3.

3. Conclusions

In summary, the excited-state landscape of the benchmark complex $[Cr(phen)_3]^{3+}$ is resolved through a combined ultrafast spectroscopy and computational investigation, as summarized in Fig. 5. High-energy excitation initially populates the ^{4}IL and ^{4}LMCT states, which undergo rapid nonradiative decay into the doublet manifold, where subsequent relaxation produces long-lived near-infrared phosphorescence. The relaxation from

the initially absorbing state to the multiconfigurational $^2T_1/^2E$ state is biexponential, resolved herein as an initial intersystem crossing to the doublet manifold followed by vibrational relaxation within it. The broad and intense $(\varepsilon^{\star}_{max} = 3000\,M^{-1}\,cm^{-1})$ excited-state absorption features and kinetics that describe this doublet state reflect a complex mixing of metal-centered, intraligand, and charge-transfer transitions. Defining these transitions supports future experimental efforts to enhance intersystem crossing yields and to design chromophore systems with high intersystem crossing efficiencies. Finally, the near-infrared phosphorescence proceeds from this metal-centered state into the ground state.

Assigning the excited-state absorption features of Cr(III) diimine complexes requires a multiconfigurational description, as single-reference approaches such as density functional theory suffer from spin contamination and an inadequate treatment of the closely spaced doublet manifold in open-shell complexes. In particular, the ESA spectrum arises from a dense manifold of states with mixed metal-centered and ligand-centered character, which cannot be captured within a single-determinant framework.

The excellent agreement between the calculated vertical excitations and the broad UV-Vis-NIR experimental ESA profiles demonstrates that RASSCF provides a quantitatively reliable description of both the energetic distribution and the character of the relevant excited states. This enables consistent assignment of spectral features and reveals the interplay among multiple electronic configurations underlying the long-lived phosphorescent state. As such, these results demonstrate that the excited-state behavior of open-shell inorganic chromophores can deviate substantially from conventional closed-shell singlet-triplet descriptions.

Together, these mechanistic and computational findings accurately reproduce the absorption and photoluminescence emission signatures of the long-lived phosphorescent state, highlighting the multiconfigurational and multimodal nature of Cr(III) photophysics, and provide a basis for rationalizing and tuning earth-abundant photofunctional chromophores.

4. Experimental section

4.1 General considerations

Air-free manipulations were conducted with Schlenk or glovebox techniques under an N_2 atmosphere. Solvents were deoxygenated by sparging N_2 gas and passing through an activated alumina column using a solvent purification system (MBraun SPS). Reagents were acquired from Ambeed, Inc., Sigma-Aldrich, or Alfa Aesar. Elemental analysis was performed by Atlantic Microlab (Norcross, GA). High-resolution mass spectrometry (HRMS) was performed using an UltiMate 3000 UHPLC system interfaced with an Exactive Plus mass spectrometer (Thermo Scientific) and processed with the FreeStyle software suite. This instrument is part of the Mass Spectrometry Core Lab in the Molecular Education, Technology, and Research Innovation Center (METRIC) facilities at NC State University. Infrared spectra were recorded on solid samples using a Bruker Platinum ATR-FTIR and processed using the OPUS software suite.

4.2 Static spectroscopy measurements

Molar extinction measurements were performed under ambient conditions in a 1 cm pathlength fused quartz cuvette sample cell using a Shimadzu UV-3600 spectrometer. Additional UV-Vis-NIR measurements were recorded using a Cary 60 spectrometer. All samples were measured with a blank solvent background. Steady-state photoluminescence measurements were collected under ambient conditions. Room temperature (295 K) steady-state photoluminescence and excitation scan measurements were recorded on an FS 5 Fluorescence Spectrometer (Edinburgh Instruments). Sample excitation was provided by an Xe arc lamp, with wavelength selection provided by a monochromator and detection provided by a visible PMT detector. Photoluminescence quantum yield (Φ_{PL}) values were recorded using an FS 920 Fluorescence Spectrometer (Edinburgh Instruments) equipped with an Xe arc lamp and PMT detector.

Emission quantum yield measurements were collected using relative emission measurements with ambient $[Ru(bpy)_3](PF_6)_2$ as a standard, employing the following formula (eqn 1):

$$\Phi_S = \Phi_R \times \left(\frac{F_S}{F_R}\right) \times \left(\frac{A_R}{A_S}\right) \times \left(\frac{n_S}{n_R}\right)^2 \quad (1)$$

where the subscripts S and R denote the sample and reference, respectively, Φ is the quantum yield of the reference under identical conditions, F is the integrated intensity of the emission signal, A represents the absorbance intensity of the solution, and n denotes the refractive index of the solvent. The standard $[Ru(bpy)_3](PF_6)_2$ has a quantum yield of $\Phi = 0.018$ in aerated CH_3CN.[76] Measurements were recorded with $A_{355\ nm} = 0.10$ in spectrophotometric grade CH_3CN.

Low-temperature (77 K) photoluminescence measurements were acquired in *n*-butyronitrile solvent (Beantown Chemical Corporation, 99%) in a 3 mm I.D. quartz EPR tube (Wilmad Glass). Measurements were performed using an FS 920 fluorimeter (Edinburgh Instruments) equipped with an Xe arc lamp and a visible PMT detector.

4.3 Electrochemistry and spectroelectrochemistry

Electrochemistry measurements were performed in a nitrogen-filled glovebox. Measurements were performed using 0.25 M tetra-*n*-butylammonium hexafluorophosphate ($[^nBu_4N][PF_6]$) electrolyte and CH_3CN solvent. Before use, $[^nBu_4N][PF_6]$ was purified by recrystallization from methanol. Measurements were performed using a sample concentration of 1 mM. Cyclic voltammetry measurements were acquired using a glassy carbon working electrode, platinum wire counter electrode, and an $Ag/AgNO_3$ reference electrode. Potentials are reported against a ferrocenium/ferrocene (Fc^+/Fc) couple (Sigma-Aldrich, 99.99%) as an internal standard. Measurements were

recorded with an Electrochemical Workstation potentiostat (CH Instruments CHI650E) and processed using OriginPro 2023*b* software.

Spectroelectrochemistry measurements were performed in 0.25 M [^{n}Bu$_4$N][PF$_6$] electrolyte in CH_3CN solvent. Potential was provided by an Electrochemical Workstation potentiostat (CH Instruments CHI650E) and processed using OriginPro 2023*b*. Measurements were recorded using a Honeycomb Spectroelectrochemistry Cell (Pine Research). The working electrode and platinum counter electrode are installed on the ceramic card, while an Ag/$AgNO_3$ reference electrode was used. Optical detection was performed with an HR2000+ spectrometer (Ocean Optics) and a UV-Vis-NIR light source (DT-MINI-2-GS) using fiber-optic cables. Measurements were recorded using the provided 1.7 mm path-length quartz cuvette.

4.4 Ultrafast transient absorption spectroscopy

Transient absorption measurements were recorded in the Imaging and Kinetics laboratory at NC State University. Femtosecond transient absorption spectroscopy (fs-TA) measurements were obtained using a Helios fs-TA spectrometer (Ultrafast Systems). A portion of the 800 nm fundamental beam output from the Ti:Sapphire amplifier (Coherent Astrella, 7 J per pulse, 100 fs fwhm) is used to generate the pump beam. The remaining portion of the 800 nm fundamental beam is directed towards a 6 ns delay stage. The white light continuum is produced using a CaF_2 crystal (350 to 800 nm) and a 10 mm sapphire crystal (800 to 1600 nm). The probe and pump beams are overlapped at the sample position. Samples are prepared in a 2 mm path length quartz cuvette (Starna Cells) using spectrophotometric-grade CH_3CN solvent. Absorption measurements are recorded before and after each transient absorption measurement to ensure there is no sample decomposition. Spectral kinetics are fit using OriginPro 2023*b*.

The excited state extinction coefficient of compound **1** was measured by comparing the excited state absorption spectrum to that of an isoabsorbant sample of [Ru(bpy)$_3$](PF$_6$)$_2$ in CH_3CN. The excited state spectrum was scaled to match the reported excited state extinction coefficient of [Ru(bpy)$_3$]$^{2+}$ in CH_3CN: $\varepsilon^*_{GSB,448\,nm} = -1.13 \times 10^4\ M^{-1}\ cm^{-1}$.[73]

4.5 Time-resolved photoluminescence spectroscopy

Nanosecond time-resolved photoluminescence measurements were obtained using an LP920 flash photolysis spectrometer (Edinburgh Instruments). Samples were prepared in a 1 cm fused quartz cuvette equipped with a Kontes Teflon cap and degassed at least 4 times using freeze-pump-thaw techniques. Samples were prepared at O.D. = 0.50 at λ_{ex} = 355 nm. Pulsed laser excitation was generated using a Vibrant LD 355 II Nd:YAG/OPO system (Edinburgh Instruments), which generated a pulse energy of 8.2 mJ per pulse. The probe beam was generated from a 450 W Xe arc lamp. Each emission spectrum was acquired using an iStar ICCD camera (Andor Technologies) and controlled with the L900 software (Edinburgh Instruments). Kinetics were fit to a single-exponential model using OriginPro 2023*b*. The ICCD detector was calibrated using the second-order diffraction scattering peak (709.4 nm).

5. Computational details

The quartet ground state of **1** was optimized using unrestricted Kohn–Sham density functional theory with the B3LYP functional[77] and the ZORA-def2-SVP basis set.[78] Since experimental data show no significant solvent dependence, gas-phase calculations were chosen to reduce computational costs. Ground-state geometry optimization and frequency calculations were performed using ORCA 5.0.4.[79] The frequency calculation was conducted to compute the normal modes at this geometry as well as confirm its identity as a minimum through the absence of imaginary frequencies (Table S1). The D3BJ correction was used to include dispersion effects.[80] Scalar relativistic effects were included using the ZORA Hamiltonian.[81] For the self-consistent-field (SCF) calculations, the resolution-of-identity approximation (RIJCOSX)[82] with def2/J auxiliary basis sets and the tight SCF convergence criteria (TightSCF) were used. No symmetry restrictions were introduced.

Multireference calculations were performed using the OpenMolcas program package version v.23.[83] The state-averaged complete-active-space self-consistent field (CASSCF),[84] restricted-active-space self-consistent field (RASSCF),[85] and multireference perturbation theory (CASPT2)[86] calculations to obtain the emission peak were performed using the ANO-RCC-VDZP basis set.[87,88] To speed up the integral calculations, the Cholesky decomposition (RICD) was employed.[89] The CASSCF/RASSCF calculations presented are done as state average (SA) with equal weights. The character assignments were based on the analysis of the transition-density matrix, calculated using the Löwdin-style approach in the TheoDORE package.[90] For states exhibiting a low degree of single-excitation character, where standard TheoDORE descriptors are less reliable, assignments were supplemented by analyzing the changes of the natural orbital populations.

Vertical excitation energies were calculated with the RASSCF(13,3,3;5,5,7) protocol, allowing up to triple excitations between RAS1/RAS3 subspaces. In RAS calculations, the notation RAS(n,l,m;i,j,k) is employed following the previous work[91] where 'n' corresponds to the total number of active electrons, 'l' and 'm' denote the maximum number of holes in RAS1 and electrons in RAS3, respectively, while 'i', 'j', and 'k' correspond to the number of orbitals in RAS1, RAS2, and RAS3 subspaces, respectively. The active space choice was guided by extensive testing on the present system. The active space includes 3 π and 2 σ orbitals in the RAS1 subspace, the full set of 3d metal orbitals in the RAS2 subspace, and 3 π* and 1 σ* orbitals as well as three 4d orbitals in the RAS3 subspace (Fig. S1). State-averaging was performed over 14 states for calculations at the quartet minima and over 30 states for the doublet manifold, what ensures a balanced description of the high-density

excited-state landscape. The vertical excitation energies are shown in Tables S2 and S3.

The geometry optimization of the doublet state minimum of **1** was done at the SA(5)-CASSCF(3;5) level of theory, due to the multiconfigurational character of the doublet state. The active space included 3 electrons in the five 3d chromium orbitals. Considering that all low-lying doublet and quartet states in the excitation calculations are of MC character, we performed emission energy calculations using CASPT2 calculations with IPEA shift 0.25 a.u. and imaginary shift of 0.4. The energy values used for calculating emission are shown in Table S4.

Author contributions

ATB and DF contributed equally to this work. ATB: investigation (synthesis and photophysics), formal analysis, and writing – original manuscript draft. IYD: investigation (electrochemistry). AF: investigation (spectroelectrochemistry). JPW: investigation (precursor synthesis). FNC: conceptualization, investigation supervision, funding acquisition, and manuscript editing. DF: theoretical calculations and analysis, manuscript editing. LG: conceptualization, theory supervision, funding acquisition, and manuscript editing. All authors have given approval to the final version of the manuscript. The manuscript was written through the contributions of all authors.

Conflicts of interest

There are no conflicts to declare.

Data availability

Supplementary information (SI): substantial details on the quantum chemical calculations and the experimental data. See DOI: **https://doi.org/10.1039/d6qi00728g**.

The raw experimental and computational data could be shared upon request.

Acknowledgements

Financial support for this project (F. N. C., A. T. B., A. P. F, I. Y. D, and J. P. W) was provided by the U.S. Department of Energy, Office of Science, Office of Basic Energy Sciences, Award Number DE-SC0011979. This work was performed in part by the Molecular Education, Technology, and Research Innovation Center (METRIC) at NC State University, which is supported by the State of North Carolina. The computational part of the research (D. F. and L. G.) was supported by the Deutsche Forschungsgemeinschaft (DFG, German Research Foundation) *via* the project GO 1059/8-2 within the SPP 2102 "Light-Controlled Reactivity of Metal Complexes" (project number 403837698) and the University of Vienna. The Austrian Scientific Cluster is acknowledged for allocation of computational resources.

References

1 C. K. Prier, D. A. Rankic and D. W. C. MacMillan, Visible light photoredox catalysis with transition metal complexes: applications in organic synthesis, *Chem. Rev.*, 2013, **113**, 5322–5363.
2 E. R. Welin, C. Le, D. M. Arias-Rotondo, J. K. McCusker and D. W. C. MacMillan, Photosensitized, energy transfer-mediated organometallic catalysis through electronically excited nickel(II), *Science*, 2017, **355**, 380–385.
3 J. M. R. Narayanam and C. R. J. Stephenson, Visible light photoredox catalysis: applications in organic synthesis, *Chem. Soc. Rev.*, 2011, **40**, 102–113.
4 J. Xuan and W. Xiao, Visible–light photoredox catalysis, *Angew. Chem., Int. Ed.*, 2012, **51**, 6828–6838.
5 D. C. Cabanero and T. Rovis, Low-energy photoredox catalysis, *Nat. Rev. Chem.*, 2024, **9**, 28–45.
6 D. M. Schultz and T. P. Yoon, Solar synthesis: prospects in visible light photocatalysis, *Science*, 2014, **343**, 1239176.
7 M. H. Shaw, J. Twilton and D. W. C. MacMillan, Photoredox catalysis in organic chemistry, *J. Org. Chem.*, 2016, **81**, 6898–6926.
8 J. Twilton, C. Le, P. Zhang, M. H. Shaw, R. W. Evans and D. W. C. MacMillan, The merger of transition metal and photocatalysis, *Nat. Rev. Chem.*, 2017, **1**, 0052.
9 D. Kim, V. Q. Dang and T. S. Teets, Improved transition metal photosensitizers to drive advances in photocatalysis, *Chem. Sci.*, 2024, **15**, 77–94.
10 J. W. Tucker and C. R. J. Stephenson, Shining light on photoredox catalysis: theory and synthetic applications, *J. Org. Chem.*, 2012, **77**, 1617–1622.
11 D. M. Arias-Rotondo and J. K. McCusker, The photophysics of photoredox catalysis: a roadmap for catalyst design, *Chem. Soc. Rev.*, 2016, **45**, 5803–5820.
12 O. S. Wenger, Photoactive complexes with earth-abundant metals, *J. Am. Chem. Soc.*, 2018, **140**, 13522–13533.
13 B. M. Hockin, C. Li, N. Robertson and E. Zysman-Colman, Photoredox catalysts based on earth-abundant metal complexes, *Catal. Sci. Technol.*, 2019, **9**, 889–915.
14 C. Förster and K. Heinze, Bimolecular reactivity of 3d metal-centered excited states (Cr, Mn, Fe, Co), *Chem. Phys. Rev.*, 2022, **3**, 041302.
15 F. Glaser and O. S. Wenger, Recent progress in the development of transition-metal based photoredox catalysts, *Coord. Chem. Rev.*, 2020, **405**, 213129.
16 J. Fajardo Jr., A. T. Barth, M. Morales, M. K. Takase, J. R. Winkler and H. B. Gray, Photoredox catalysis mediated by tungsten (0) arylisocyanides, *J. Am. Chem. Soc.*, 2021, **143**, 19389–19398.
17 A. T. Barth, J. Fajardo Jr., W. Sattler, J. R. Winkler and H. B. Gray, Electronic Structures and Photoredox Chemistry

of Tungsten (0) Arylisocyanides, *Acc. Chem. Res.*, 2023, **56**, 1978–1989.
18 A. T. Barth, M. Morales, J. R. Winkler and H. B. Gray, Photoredox Catalysis Mediated by Tungsten (0) Arylisocyanides in 1, 2-Difluorobenzene, *Inorg. Chem.*, 2022, **61**, 7251–7255.
19 R. F. Higgins, S. M. Fatur, S. G. Shepard, S. M. Stevenson, D. J. Boston, E. M. Ferreira, N. H. Damrauer, A. K. Rappé and M. P. Shores, Uncovering the roles of oxygen in Cr(III) photoredox catalysis, *J. Am. Chem. Soc.*, 2016, **138**, 5451–5464.
20 R. F. Higgins, S. M. Fatur, N. H. Damrauer, E. M. Ferreira, A. K. Rappé and M. P. Shores, Detection of an energy-transfer pathway in Cr-photoredox catalysis, *ACS Catal.*, 2018, **8**, 9216–9225.
21 S. M. Stevenson, R. F. Higgins, M. P. Shores and E. M. Ferreira, Chromium photocatalysis: accessing structural complements to Diels–Alder adducts with electron-deficient dienophiles, *Chem. Sci.*, 2017, **8**, 654–660.
22 S. M. Stevenson, M. P. Shores and E. M. Ferreira, Photooxidizing chromium catalysts for promoting radical cation cycloadditions, *Angew. Chem., Int. Ed.*, 2015, **54**, 6506–6510.
23 B. K. Gall, A. K. Smith and E. M. Ferreira, Dearomative (3 + 2) Cycloadditions between Indoles and Vinyldiazo Species Enabled by a Red–Shifted Chromium Photocatalyst, *Angew. Chem., Int. Ed.*, 2022, **61**, e202212187.
24 F. J. Sarabia, Q. Li and E. M. Ferreira, Cyclopentene annulations of alkene radical cations with vinyl diazo species using photocatalysis, *Angew. Chem., Int. Ed.*, 2018, **57**, 11015–11019.
25 F. J. Sarabia and E. M. Ferreira, Radical cation cyclopropanations via chromium photooxidative catalysis, *Org. Lett.*, 2017, **19**, 2865–2868.
26 T. H. Bürgin, F. Glaser and O. S. Wenger, Shedding Light on the Oxidizing Properties of Spin-Flip Excited States in a Cr^{III} Polypyridine Complex and Their Use in Photoredox Catalysis, *J. Am. Chem. Soc.*, 2022, **144**, 14181–14194.
27 S. Sittel, D. Zorn, A. König, J. M. Grenz, C. Förster, R. Naumann and K. Heinze, Decoupling Redox Potentials and Excited State Energies in Substituted Chromium(III) Chromophores, *Chem. – Eur. J.*, 2025, e02668.
28 S. Sittel, J. Neuner, J. M. Grenz, C. Förster, R. Naumann and K. Heinze, Gram–Scale Photocatalysis with a Stable and Recyclable Chromium(III) Photocatalyst in Acetonitrile and in Water, *Adv. Synth. Catal.*, 2025, **367**, e202500075.
29 G. Morselli, T. H. Eggenweiler, M. Villa, A. Prescimone and O. S. Wenger, Pushing the Thermodynamic and Kinetic Limits of Near-Infrared Emissive Cr^{III} Complexes in Photocatalysis, *J. Am. Chem. Soc.*, 2025, **147**, 28226–28240.
30 N. Arai and T. Ohkuma, Photochemically promoted Aza-Diels–Alder-type reaction: High catalytic activity of the Cr (III)/bipyridine complex enhanced by visible light irradiation, *J. Org. Chem.*, 2017, **82**, 7628–7636.
31 S. Otto, A. M. Nauth, E. Ermilov, N. Scholz, A. Friedrich, U. Resch-Genger, S. Lochbrunner, T. Opatz and K. Heinze, Photo–Chromium: Sensitizer for Visible–Light–Induced Oxidative C– H Bond Functionalization—Electron or Energy Transfer?, *ChemPhotoChem*, 2017, **1**, 344–349.
32 S. Sittel, A. C. Sell, K. Hofmann, C. Wiedemann, J. P. Nau, C. Kerzig, G. Manolikakes and K. Heinze, Visible–Light Induced Fixation of SO_2 into Organic Molecules with Polypyridine Chromium(III) Complexes, *ChemCatChem*, 2023, **15**, e202201562.
33 C. Wang, F. Reichenauer, W. R. Kitzmann, C. Kerzig, K. Heinze and U. Resch-Genger, Efficient Triplet–Triplet Annihilation Upconversion Sensitized by a Chromium(III) Complex via an Underexplored Energy Transfer Mechanism, *Angew. Chem., Int. Ed.*, 2022, **61**, e202202238.
34 B. Brunschwig and N. Sutin, Reactions of the excited states of substituted polypyridinechromium(III) complexes with oxygen, iron(II) ions, ruthenium(II) and -(III), and osmium (II) and -(III) complexes, *J. Am. Chem. Soc.*, 1978, **100**, 7568–7577.
35 B. S. Brunschwig, P. J. DeLaive, A. M. English, M. Goldberg, H. B. Gray, S. L. Mayo and N. Sutin, Kinetics and mechanisms of electron transfer between blue copper proteins and electronically excited chromium and ruthenium polypyridine complexes, *Inorg. Chem.*, 1985, **24**, 3743–3749.
36 N. Sinha, J. Jiménez, B. Pfund, A. Prescimone, C. Piguet and O. S. Wenger, A near–infrared–II emissive chromium (III) complex, *Angew. Chem., Int. Ed.*, 2021, **60**, 23722–23728.
37 Y. Ye, M. Poncet, P. Yaltseva, P. Salcedo-Abraira, A. Rodríguez-Diéguez, J. H. Martín, L. Cuevas-Contreras, C. M. Cruz, B. Doistau, C. Piguet, O. S. Wenger, J. M. Herrera and J.-R. Jiménez, Modulating the spin–flip rates and emission energies through ligand design in chromium(III) molecular rubies, *Chem. Sci.*, 2025, **16**, 5205–5213.
38 W. R. Kitzmann, C. Ramanan, R. Naumann and K. Heinze, Molecular ruby: exploring the excited state landscape, *Dalton Trans.*, 2022, **51**, 6519–6525.
39 C. Wang, S. Otto, M. Dorn, E. Kreidt, J. Lebon, L. Sršan, P. Di Martino-Fumo, M. Gerhards, U. Resch–Genger, M. Seitz and K. Heinze, Deuterated molecular ruby with record luminescence quantum yield, *Angew. Chem., Int. Ed.*, 2018, **57**, 1112–1116.
40 S. Treiling, C. Wang, C. Förster, F. Reichenauer, J. Kalmbach, P. Boden, J. P. Harris, L. M. Carrella, E. Rentschler, U. Resch-Genger, C. Reber, M. Seitz, M. Gerhards and K. Heinze, Luminescence and light–driven energy and electron transfer from an exceptionally long–lived excited state of a non–innocent chromium(III) complex, *Angew. Chem., Int. Ed.*, 2019, **58**, 18075–18085.
41 L. Stein, C. Förster and K. Heinze, Luminescent Cyclometalated Chromium(III) Complexes, *Organometallics*, 2024, **43**, 1766–1774.
42 S. Sittel, R. Naumann and K. Heinze, Molecular Rubies in Photoredox Catalysis, *Front. Chem.*, 2022, **10**, 887439.
43 S. Otto, M. Grabolle, C. Förster, C. Kreitner, U. Resch-Genger and K. Heinze, $[Cr(ddpd)_2]^{3+}$: A Molecular, Water–

Soluble, Highly NIR–Emissive Ruby Analogue, *Angew. Chem., Int. Ed.*, 2015, **54**, 11572–11576.

44 B. Doistau, G. Collet, E. A. Bolomey, V. Sadat-Noorbakhsh, C. Besnard and C. Piguet, Heteroleptic Ter–Bidentate Cr (III) Complexes as Tunable Optical Sensitizers, *Inorg. Chem.*, 2018, **57**, 14362–14373.

45 J.-R. Jiménez, B. Doistau, M. Poncet and C. Piguet, Heteroleptic trivalent chromium in coordination chemistry: Novel building blocks for addressing old challenges in multimetallic luminescent complexes, *Coord. Chem. Rev.*, 2021, **434**, 213750.

46 M. Poncet, L. Cuevas-Contreras, Y. Ye, L. Guénée, C. M. Cruz, C. Piguet and J.-R. Jiménez, Exploring the role of the nephelauxetic effect in circularly polarized luminescence of chiral chromium (III) complexes, *J. Am. Chem. Soc.*, 2025, **147**, 23827–23833.

47 A. M. McDaniel, H.-W. Tseng, N. H. Damrauer and M. P. Shores, Synthesis and solution phase characterization of strongly photooxidizing heteroleptic Cr(III) tris-dipyridyl complexes, *Inorg. Chem.*, 2010, **49**, 7981–7991.

48 F. Reichenauer, C. Wang, C. Forster, P. Boden, N. Ugur, R. Báez-Cruz, J. Kalmbach, L. M. Carrella, E. Rentschler and C. Ramanan, Strongly Red-Emissive Molecular Ruby $[Cr(bpmp)_2]^{3+}$ Surpasses $[Ru(bpy)_3]^{2+}$, *J. Am. Chem. Soc.*, 2021, **143**, 11843–11855.

49 E. A. Juban and J. K. McCusker, Ultrafast dynamics of ^2E state formation in $Cr(acac)_3$, *J. Am. Chem. Soc.*, 2005, **127**, 6857–6865.

50 N. Serpone, M. Jamieson, M. Henry, M. Hoffman, F. Bolletta and M. Maestri, Excited-state behavior of polypyridyl complexes of chromium(III), *J. Am. Chem. Soc.*, 1979, **101**, 2907–2916.

51 S. J. Milder, J. S. Gold and D. S. Kliger, Assignments of ground- and excited-state spectra from time-resolved absorption and circular dichroism measurements of the ^2E state of (Δ)-$[Cr(bpy)_3]^{3+}$, *Inorg. Chem.*, 1990, **29**, 2506–2511.

52 J. P. Zobel, H. Radatz and L. González, Photodynamics of the Molecular Ruby $[Cr(ddpd)_2]^{3+}$, *Molecules*, 2023, **28**, 1668.

53 G. Yang, G. E. Shillito, P. Seeber, O. S. Wenger and S. Kupfer, Unraveling the photoredox chemistry of a molecular ruby, *Chem. Sci.*, 2025, **16**, 18113–18125.

54 E. A. Juban, A. L. Smeigh, J. E. Monat and J. K. McCusker, Ultrafast dynamics of ligand-field excited states, *Coord. Chem. Rev.*, 2006, **250**, 1783–1791.

55 E. A. Juban, *The Ultrafast Dynamics of Chromium(III) Coordination Complexes*, PhD Thesis, University of California, Berkeley, 2006.

56 A. D. Kirk, Photochemistry and photophysics of chromium (III) complexes, *Chem. Rev.*, 1999, **99**, 1607–1640.

57 J. P. Joyce, R. I. Portillo, C. M. Nite, J. M. Nite, M. P. Nguyen, A. K. Rappe and M. P. Shores, Electronic structures of Cr(III) and V(II) polypyridyl systems: Undertones in an isoelectronic analogy., *Inorg. Chem.*, 2021, **60**, 12823–12834.

58 M. A. Jamieson, N. Serpone and M. Z. Hoffman, Advances in the photochemistry and photophysics of chromium(III) polypyridyl complexes in fluid media, *Coord. Chem. Rev.*, 1981, **39**, 121–179.

59 N. Serpone, M. A. Jamieson, R. Sriram and M. Z. Hoffman, Photophysics and photochemistry of polypyridyl complexes of chromium(III), *Inorg. Chem.*, 1981, **20**, 3983–3988.

60 J. F. Endicott, R. B. Lessard, D. Lynch, M. W. Perkovic and C. K. Ryu, Stereochemical and electronic contributions to ^2E chromium (III) excited state relaxation behavior at 77K, *Coord. Chem. Rev.*, 1990, **97**, 65–79.

61 C. K. Ryu and J. F. Endicott, Synthesis, Spectroscopy, and Photophysical Behavior of Mixed-Ligand Mono- and Bis (polypyridyl)chromium(III) Complexes. Examples of Efficient, Thermally Activated Excited-State Relaxation without Back Intersystem Crossing, *Inorg. Chem.*, 1988, **27**, 2203–2214.

62 R. W. Jones, R. A. Cowin, I. I. Ivalo, D. Chekulaev, T. M. Roseveare, C. R. Rice, J. A. Weinstein, P. I. P. Elliott and P. A. Scattergood, A Near-Infrared Luminescent Cr(III) *N*-Heterocyclic Carbene Complex, *Inorg. Chem.*, 2024, **63**, 8526–8530.

63 R. W. Jones, A. J. Auty, G. Wu, P. Persson, M. V. Appleby, D. Chekulaev, C. R. Rice, J. A. Weinstein, P. I. P. Elliott and P. A. Scattergood, Direct determination of the rate of intersystem crossing in a near-IR luminescent Cr(III) triazolyl complex, *J. Am. Chem. Soc.*, 2023, **145**, 12081–12092.

64 W. R. Kitzmann, J. Moll and K. Heinze, Spin-flip luminescence, *Photochem. Photobiol. Sci.*, 2022, **21**, 1309–1331.

65 T. H. Bürgin, F. Glaser and O. S. Wenger, Shedding Light on the Oxidizing Properties of Spin-Flip Excited States in a Cr^{III} Polypyridine Complex and Their Use in Photoredox Catalysis, *J. Am. Chem. Soc.*, 2022, **144**, 14181–14194.

66 L. Stein, P. Boden, R. Naumann, C. Förster, G. Niedner-Schatteburg and K. Heinze, The overlooked NIR luminescence of $Cr(ppy)_3$, *Chem. Commun.*, 2022, **58**, 3701–3704.

67 N. Serpone, M. A. Jamieson, D. K. Sharma, R. Danesh, F. Bolletta and M. Z. Hoffman, Picosecond laser spectroscopy of chromium(III) complexes. Probing the photophysics of $^4T_2$ excited states of $Cr(bpy)_3^{3+}$ and $Cr(4,7\text{-}Me_2phen)_3^{3+}$ ions in aqueous solution, *Chem. Phys. Lett.*, 1984, **104**, 87–92.

68 L. S. Forster, The photophysics of chromium(III) complexes, *Chem. Rev.*, 1990, **90**, 331–353.

69 J. N. Schrauben, K. L. Dillman, W. F. Beck and J. K. McCusker, Vibrational coherence in the excited state dynamics of $Cr(acac)_3$: probing the reaction coordinate for ultrafast intersystem crossing, *Chem. Sci.*, 2010, **1**, 405.

70 C. C. Scarborough, S. Sproules, T. Weyhermüller, S. DeBeer and K. Wieghardt, Electronic and Molecular Structures of the Members of the Electron Transfer Series $[Cr(tbpy)_3]^n$ (n = 3+, 2+, 1+, 0): An X-ray Absorption Spectroscopic and Density Functional Theoretical Study, *Inorg. Chem.*, 2011, **50**, 12446–12462.

71 K. Andersson and B. O. Roos, Excitation energies in the nickel atom studied with the complete active space SCF method and second-order perturbation theory, *Chem. Phys. Lett.*, 1992, **191**, 507–514.

72 K. Pierloot and S. Vancoillie, Relative energy of the high-($^5T_{2g}$) and low-($^1A_{1g}$) spin states of $[Fe(H_2O)_6]^{2+}$,$[Fe(NH_3)_6]^{2+}$, and $[Fe(bpy)_3]^{2+}$: CASPT2 versus density functional theory, *J. Chem. Phys.*, 2006, **125**, 124303.

73 P. Müller and K. Brettel, $[Ru(bpy)_3]^{2+}$ as a reference in transient absorption spectroscopy: differential absorption coefficients for formation of the long-lived ^{3}MLCT excited state, *Photochem. Photobiol. Sci.*, 2012, **11**, 632–636.

74 L. S. Forster, Intersystem crossing in transition metal complexes, *Coord. Chem. Rev.*, 2006, **250**, 2023–2033.

75 L. S. Forster, Thermal relaxation in excited electronic states of d^3 and d^6 metal complexes, *Coord. Chem. Rev.*, 2002, **227**, 59–92.

76 K. Suzuki, A. Kobayashi, S. Kaneko, K. Takehira, T. Yoshihara, H. Ishida, Y. Shiina, S. Oishi and S. Tobita, Reevaluation of absolute luminescence quantum yields of standard solutions using a spectrometer with an integrating sphere and a back-thinned CCD detector, *Phys. Chem. Chem. Phys.*, 2009, **11**, 9850–9860.

77 A. D. Becke, Density–functional thermochemistry. III. The role of exact exchange, *J. Chem. Phys.*, 1993, **98**, 5648–5652.

78 D. A. Pantazis, X.-Y. Chen, C. R. Landis and F. Neese, All-electron scalar relativistic basis sets for third-row transition metal atoms, *J. Chem. Theory Comput.*, 2008, **4**, 908–919.

79 F. Neese, Calculation of exchange couplings in the electronically excited state of molecular three-spin systems, *Wiley Interdiscip. Rev.: Comput. Mol. Sci.*, 2022, **12**, e1606.

80 S. Grimme, J. Antony, S. Ehrlich and H. Krieg, A consistent and accurate ab initio parametrization of density functional dispersion correction (DFT-D) for the 94 elements H-Pu Available to Purchase, *J. Chem. Phys.*, 2010, **132**, 154104.

81 C. van Wüllen, Molecular density functional calculations in the regular relativistic approximation: Method, application to coinage metal diatomics, hydrides, fluorides and chlorides, and comparison with first-order relativistic calculations, *J. Chem. Phys.*, 1998, **109**, 392–399.

82 F. Neese, F. Wennmohs, A. Hansen and U. Becker, Efficient, approximate and parallel Hartree–Fock and hybrid DFT calculations. A 'chain-of-spheres' algorithm for the Hartree–Fock exchange, *Chem. Phys.*, 2009, **356**, 98–109.

83 G. Li Manni, I. F. Galván, A. Alavi, F. Aleotti, F. Aquilante, J. Autschbach, D. Avagliano, A. Baiardi, J. J. Bao, S. Battaglia, *et al.*, The OpenMolcas *Web*: A Community-Driven Approach to Advancing Computational Chemistry, *J. Chem. Theory Comput.*, 2023, **19**, 6933–6991.

84 B. O. Roos, P. R. Taylor and P. E. M. Sigbahn, A complete active space SCF method (CASSCF) using a density matrix formulated super-CI approach, *Chem. Phys.*, 1980, **48**, 157–173.

85 P.-Å. Malmqvist, A. Rendell and B. O. Roos, The restricted active space self-consistent-field method, implemented with a split graph unitary group approach, *J. Phys. Chem. A*, 1990, **94**, 5477–5482.

86 J. Finley, P.-Å. Malmqvist, B. O. Roos and L. Serrano-Andrés, The multi-state CASPT2 method, *Chem. Phys. Lett.*, 1998, **288**, 299–306.

87 B. O. Roos, R. Lindh, P.-Å. Malmqvist, V. Veryazov and P.-O. Widmark, New relativistic ANO basis sets for transition metal atoms, *J. Phys. Chem. A*, 2005, **109**, 6575–6579.

88 B. O. Roos, R. Lindh, P.-Å. Malmqvist, V. Veryazov and P.-O. Widmark, Main group atoms and dimers studied with a new relativistic ANO basis set, *J. Phys. Chem. A*, 2004, **108**, 2851–2858.

89 F. Aquilante, R. Lindh and T. B. Pedersen, Unbiased auxiliary basis sets for accurate two-electron integral approximations, *J. Chem. Phys.*, 2007, **127**, 114107.

90 F. Plasser, TheoDORE: A toolbox for a detailed and automated analysis of electronic excited state computations, *J. Chem. Phys.*, 2020, **152**, 084108.

91 D. Escudero and L. González, RASPT2/RASSCF vs Range-Separated/Hybrid DFT Methods: Assessing the Excited States of a Ru(II)bipyridyl Complex, *J. Chem. Theory Comput*, 2012, **8**, 203–213.